Journal Pre-proof

Long-range and short-range ordering in 2D honeycomb-lattice magnet $Na_2Ni_2TeO_6$

Alexander I. Kurbakov, Artem N. Korshunov, Stanislav Yu Podchezertsev, Mikhail I. Stratan, Grigory V. Raganyan, Elena A. Zvereva

PII: S0925-8388(19)34600-6

DOI: https://doi.org/10.1016/j.jallcom.2019.153354

Reference: JALCOM 153354

To appear in: *Journal of Alloys and Compounds*

Received Date: 19 July 2019

Revised Date: 7 November 2019

Accepted Date: 9 December 2019

Please cite this article as: A.I. Kurbakov, A.N. Korshunov, S.Y. Podchezertsev, M.I. Stratan, G.V. Raganyan, E.A. Zvereva, Long-range and short-range ordering in 2D honeycomb-lattice magnet $Na_2Ni_2TeO_6$, *Journal of Alloys and Compounds* (2020), doi: https://doi.org/10.1016/j.jallcom.2019.153354.

Long-range and short-range ordering in 2D honeycomb-lattice magnet $Na_2Ni_2TeO_6$

Alexander I. Kurbakov[1,2], Artem N. Korshunov[1,2], Stanislav Yu. Podchezertsev[1], Mikhail I. Stratan[3], Grigory V. Raganyan[3], Elena A. Zvereva[3]

[1]*NRC «Kurchatov Institute» - PNPI, 188300 Gatchina, Russia*

[2]*Faculty of Physics, St.Petersburg State University, 198504 St. Petersburg, Russia*

[3]*Faculty of Physics, M.V. Lomonosov Moscow State University, 119991 Moscow, Russia*

(Dated: XX July 2019)

Abstract

The magnetic structure of quasi-two-dimensional (2D) honeycomb lattice $Na_2Ni_2TeO_6$ has been determined by low-temperature neutron diffraction and the crystal structure fine details at room temperature have been established by a combination of synchrotron and neutron powder diffraction. The atomic structure is described by the *P6₃/mcm* space group, but the strong presence of stacking faults defects in layered ordering is found for the first time. Both magnetization and specific heat data indicates an establishment of a long-range antiferromagnetic order with T_N = 25±1 K, preceded by a short-range order on 2D honeycomb lattice at about 34 K. Determined effective magnetic moment μ_{eff} = 4.35 μ_B is in excellent agreement with numerical estimation using effective g-factor g = 2.19 directly measured by electron spin resonance. The ground magnetic state at T = 1.5 K is represented by the commensurate zigzag-type magnetic order. Magnetic moments of Ni are almost perpendicular to the honeycomb layers, which antiferromagnetically coupled along the *c*-direction. Besides, the coherent magnetic scattering area has a disk shape that is homogeneous over the *ab* plane and compressed along the *c*-axis that indicates 2D nature of magnetic correlations in the compound. The magnetic diffuse neutron scattering related to the presence of strong short-range spin-spin correlations above T_N was observed. Based on our experimental measurements we propose magnetic phase diagram for $Na_2Ni_2TeO_6$.

Keywords: low dimensional magnetism, honeycomb lattice, neutron scattering, zigzag-type spin structure, magnetic phase diagram

*Corresponding author. E-mail: kurbakov_ai@pnpi.nrcki.ru.

1. Introduction

Presently, low-dimensional magnetism is a subject of considerable interest in condensed matter physics because of plenty of new interesting phenomena that can be studied on strongly correlated spin systems. A large number of various non-trivial magnetic states can be realized in view of reduced spatial dimension and small spin value ($S \leq 1$) when the quantum effects take place. The nature of the magnetic state depends on the spin-spin couplings and the presence of frustration and anisotropy. The low-dimensional magnets represented by the bulk materials have special attention since the influence of boundary effects can be excluded from consideration.

Recently, the new examples of such systems with the general formula $A^{1+}{}_2M^{2+}{}_2X^{6+}O_6$ and $A^{1+}{}_3M^{2+}{}_2X^{5+}O_6$ (A = Li, Na, K….; M = Mn, Fe, Co, Ni, Cu …., X = Te, Sb, Bi) began to be actively studied [1-9]. They represent the layered structures formed by honeycomb ordered magnetically active layers alternating alkali metal atoms. This arrangement leads to a certain softness of the crystal structure in the perpendicular layers packing direction, therefore different ways of stacking the honeycomb layers against each other and the possibility of breaking these layouts through a certain number of layers can be implemented. The structure of individual honeycomb magnetic layer is very rigid that is very important in view of magnetism.

Due to the high demand for such compounds in electrochemistry, numerous studies of their transport, thermoelectric, electrochemical, and other properties and characteristics were carried out in recent years [9-11]. The number of studies on their magnetic properties is also dramatically increasing for obvious reasons. These compounds belong to the class of natural quasi-two-dimensional magnets with hexagonally ordered magnetic atoms in layers. According to the J_1 - J_2 - J_3 theoretical model [12-14], where competition of exchange interactions between first, second, and third nearest magnetic neighbors is taken into account, the different magnetic ground states known as zigzag, stripe, and spiral ordering can be realized on the honeycomb net. Besides, the edge-sharing oxygen octahedral arrangements of transition metals lead to a complex scheme of magnetic interaction in system, that mainly determined by orbital degrees of freedom on the honeycomb net. The special attention deserves the possibility of the quantum spin liquid state, where long-range magnetic ordering can be suppressed by presence of frustration or anisotropic exchange interactions. In particular, Kitaev proposed an exactly solvable model for two-dimensional honeycomb lattice of spins S = ½ with bond-dependent couplings, which suggest the Majorana-like fractional spin excitations [15]. A promising result for Kitaev model realization was received for d^5 transition metals-based insulators with strong spin-orbit coupling [16, 17]. However zigzag-type antiferromagnetic ordering for α-$RuCl_3$ [18] and Na_2IrO_3 [19-21] was experimentally observed by means neutron diffraction measurements at low temperature. It was shown that the observed result is a consequence of the competition between anisotropic

Kitaev interactions and isotropic Heisenberg interactions including next-nearest magnetic neighbors [17, 18, 21-23]. At the moment, the numerous theoretical and few experimental studies of 4d and 5d materials with S = ½ have shown that the implementation of purely Kitaev interactions may not be feasible in any real material, but advanced models, including more realistic interactions, contain many interesting states and own phenomena [24].

In the last year, attempts to extend the Kitaev model in two directions, both on 3d transition metal-based materials, and systems with higher spins were began. In particular, cobaltates with d^7 ions Co^{2+} can possess pseudospin-1/2 ground state formed by the $t^5_{2g}e^2_g$ electron configuration with total spin S = 3/2 and effective angular moment L = 1 [25]. The resulting Hamiltonian contains bond-directional Kitaev and Heisenberg isotropic interactions, as in the case of d^5 ions. It is important to note that the presence of additional spin-active e_g electrons in d^7 cobaltates radically changes the balance between Kitaev and Heisenberg couplings that directly effects on the corresponding phase diagram. If the system belongs to the charge transfer mode ($U > \Delta$), which is indeed the case for many cobalt compounds, then the Heisenberg antiferromagnetic coupling J is strongly suppressed, and the spin-liquid phase can be stabilized. The results show that cobalt-based materials are promising candidates for the implementation of the Kitaev model, and it is specifically offered to pay attention to $Na_2Co_2TeO_6$ and $Na_3Co_2SbO_6$ compounds with a layered hexagonal structure in which d^7 Co^{2+} ions form a nearly perfect honeycomb lattice and develop an antiferromagnetic zigzag-type order at low temperatures, similar to that observed in d^5 pseudospin-1/2 $RuCl_3$ and Na_2IrO_3 materials. A similar approach was also offered in [26]. Moreover, in [27] a possibility of the spin S = 1 Kitaev model in two dimensional edge-shared octahedral systems was presented. Bond-dependent Kitaev interactions realize via superexchange couplings between half-filled cation e_g orbitals mediated by anion p orbital. To achieve this mechanism two essential ingredients are noted: the system should have strong Hund's coupling among two electrons in the transition metal cations and strong spin-orbit coupling (SOC) at anion sites. Taking into account the antiferromagnetic Heisenberg term from direct-exchange paths, the Kitaev interaction dominates the physics of S = 1 system and the gapless spin liquid state can be expected. In [27], the $A_3Ni_2XO_6$ composition is considered as a promising candidate for the implementation of the high-spin Kitaev physics. Moreover, the 2D honeycomb layer arrangements in the $A_3Ni_2XO_6$ is isostructural to the less studied $Na_2Ni_2TeO_6$ composition and we should expect similar effects in this case.

The present work is devoted to the study of quasi-two-dimensional magnetism on the example of $Na_2Ni_2TeO_6$ layered compound with honeycomb ordering of the magnetic atoms in the layer. Only the crystal structure and some macromagnetic properties were reported

previously for this composition [9, 28, 29]. All this, along with neutron diffraction data led to the conclusion about the antiferromagnetic phase transition at low temperature. However, the details of the magnetic ground state in $Na_2Ni_2TeO_6$ and its evolution at temperature remain unclear. In this paper, we report on the crystal and magnetic structure, static and dynamic magnetic properties from the point of view of the long-range magnetic order formation mechanisms. Based on the thermodynamic data on the field and temperature dependences of the magnetization, as well as on the specific heat, we construct a magnetic phase diagram for $Na_2Ni_2TeO_6$. The zigzag-type magnetic order with the spins that are almost perpendicular to the honeycomb layers is determined for the magnetic ground state. A transition from the paramagnetic to the antiferromagnetic phase takes place at 25 K, but prior this strong short-range ordering effect is observed.

2. Experimental

Polycrystalline samples were prepared by standard solid-state reactions as was early reported in [9].

Magnetic measurements were performed by means of VSM option of a Quantum Design PPMS-9 system. The magnetic susceptibility data were taken over the temperature range 2–50 K in applied fields up to 9 T and in the temperature range 2–300 K at $B = 1$ T. The isothermal magnetization curves were obtained in static magnetic fields $B \leq 9$ T and at $T \leq 25$ K after cooling the sample in zero magnetic field.

The specific heat measurements were carried out by a relaxation method using a Quantum Design PPMS-9 system. The plate-shaped samples of $Na_2Ni_2TeO_6$ and its non-magnetic analogue $Na_2Zn_2TeO_6$ of ≈ 0.2 mm thickness and ≈ 8 mg mass were obtained by cold pressing of the polycrystalline powder. Data were collected at zero magnetic field and under applied fields up to 9 T in the temperature range 2 – 100 K.

Electron spin resonance (ESR) studies were carried out using an X-band ESR spectrometer CMS 8400 (ADANI) (f ~ 9.4 GHz, $B \leq 0.7$ T) equipped with a low-temperature mount, operating in the range $T = 6$–300 K. The effective g-factor of our sample has been calculated with respect to an external reference for the resonance field. We used BDPA (*a*,*g*-bisdiphenyline-*b*-phenylallyl) $g_{ref} = 2.00359$, as a reference material.

High-resolution room temperature (RT) neutron powder diffraction was performed on the SSPD diffractometer located at WWR-M reactor (PNPI, Gatchina, Russian Federation). Monochromatic neutron beam with a wavelength λ = 1.752 Å was obtained with a focusing

(004) germanium single crystal monochromator. The data were collected with a step of 0.1º in the 2θ region 12º - 158º.

Structural investigation at room temperature was carried out using the high-resolution X-ray diffractometer ID31 (now this diffractometer moved and reconstructed to ID22 beamline) at the ESRF, Grenoble, France. Monochromatic synchrotron radiation with a wavelength of 0.3999 Å was used. Diffraction data were collected in 2θ range from -12º to + 43º with step of 0.003º. The exact zero angle of the diffractometer was determined by comparing positions of the same reflections with positive and negative scattering angles. For Rietveld analysis, we used the diffraction pattern in the angular range from 4º to 43º.

The low-temperature neutron powder diffraction studies were carried out on the cold neutron two-axis G4.1 diffractometer (LLB, Saclay, France) which has a high resolution at a small diffraction angles and perfectly adapted for magnetic structure determination. The wavelength of the incident neutrons was 2.422 Å. The neutron diffraction patterns were measured in the angular range 2θ = 7º - 87º with a step of 0.1º. Rietveld refinement of all neutron and synchrotron diffraction data for determination of crystal and magnetic structures was carried out using FullProf Suite [30, 31].

3. Results

3.1. Crystal structure

The compounds of $Na_2M_2TeO_6$ family, where M = Co, Zn, Mg, have crystal ordering with *P6$_3$22* space group that was found by means of X-Ray and neutron diffraction [5, 9]. However, another *P6$_3$/mcm* space group was proposed and used in subsequent works [28, 29] for the related compound with M = Ni. Now we present the fine details of the $Na_2Ni_2TeO_6$ crystal ordering that were determined using neutron and high-resolution synchrotron powder diffraction.

Results of Rietveld analysis of the neutron diffraction pattern at RT are shown in Fig. 1. Besides the main phase, the refinement revealed additional diffraction peaks appearing from a small amount of undefined impurity. The subsequent analysis of all diffraction data together with the results of measurement of the studied compound by other physical methods, given in this article, allows us to state that the presence of this nonmagnetic impurity does not have any effect on the accuracy of the obtained characteristics.

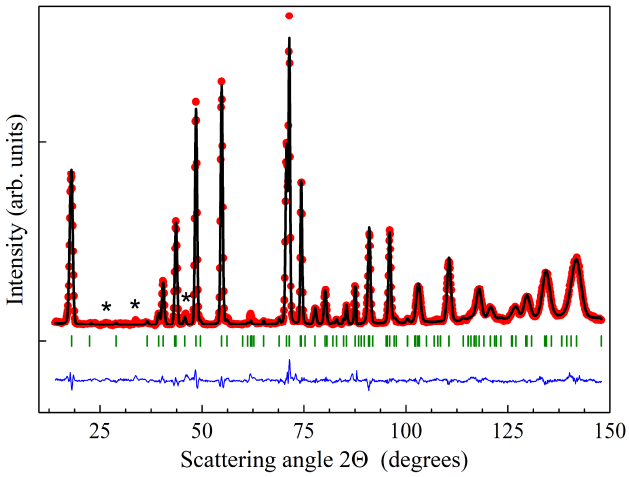

Fig. 1. RT neutron diffraction pattern of $Na_2Ni_2TeO_6$. Red circles are experimental data, black solid line is calculated profile, vertical bars are positions of Bragg peaks, blue solid line is difference curve shifted down for convenience, and asterisks mark positions of additional peaks from undefined impurity.

The best fitting corresponds to the crystal structure description within the *P6₃/mcm* space group with the refined parameters given in Table 1. The $Na_2Ni_2TeO_6$ is formed by edge-sharing NiO_6 and TeO_6 octahedra that implement perfectly ordered honeycomb layers in the *ab*-plane (Fig. 2a). Principal interatomic bondings and valence angles are listed in Table 2.

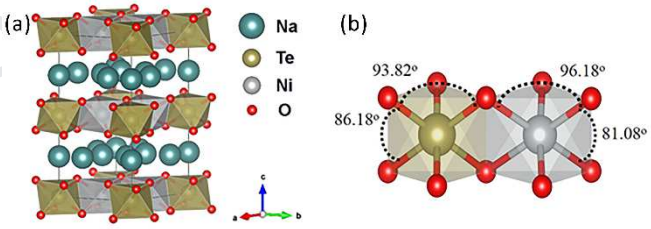

Fig. 2. a) Crystal structure of $Na_2Ni_2TeO_6$; b) fragment of a honeycomb layer.

Table 1. Crystallographic data for $Na_2Ni_2TeO_6$ in *P6₃/mcm* (#193) from neutron powder diffraction at room temperature. $a = b = 5.2016(1)$, $c = 11.1723(3)$, V = 261.791(8) Å^3. Anisotropic thermal parameters for Na atoms: $U_{11} = 0.06(6)$ Å^2, $U_{22} = 0.130(15)$ Å^2, $U_{33} = 0.016(4)$ Å^2, $U_{13} = 0.06(5)$ Å^2. Agreement factors are $R_p = 3.96$ %, $R_{wp} = 5.45$ %, $R_{exp} = 2.39$ %; global $\chi^2 = 5.22$.

Atom	Site	*x/a*	*y/b*	*z/c*	U_{iso}, Å^2	Occupancy
Te	2b	0	0	0	0.0061(12)	1
Ni	4d	2/3	1/3	0	0.0289(6)	1
O	12k	0.6816(5)	0.6816(5)	0.5945(1)	0.0259(3)	1

Na1	6g	0.347(3)	0	1/4	-//-	0.49 (69%)
Na2	4c	1/3	2/3	1/4	-//-	0.33 (31%)
Na3	2a	0	0	1/4	-//-	0 (0%)

Table 2. Selected interatomic distances and bond angles at room temperature

Bond distances (Å)		Bond angles (deg.)	
Te – O	1.964(3)		
Sum of radii [32]	1.96	O – Te – O	86.18(6)
		O – Te – O	93.82(10)
Ni – O	2.064(3)		
Sum of radii [32]	2.09		
Na1 – O	2.456(6)		
Na2 – O	2.483(2)	O – Ni – O	81.08(9)
Sum of radii [32]	2.42	O – Ni - O	96.18(9)
Ni – Ni			
First neighbors	3.003 x3		
Second neighbors	5.202 x6	Ni – O – Ni	93.34(9)
Third neighbor	6.006 x3		
Interlayer	5.586		

P6₃/mcm space group, because of the presence of only one position for all ions except Na, excludes the possibility of the difference in the bond lengths both for Ni-O and Te-O bonds, however reduced value of Ni-O bond distance in comparison to the sum of ionic radii [32] may indirectly indicate a disorder in the 3d-metal subsystem. We did not find any Ni/Te mixing in the sample as well as mixing between 3d- and alkali metals. Values of O-Ni-O (96.18º) and O-Te-O (93.82º) bond angles that are directed out of the honeycomb plane are larger than angles directed into the plane (O-Ni-O = 81.08º, O-Te-O = 86.18º), so Ni_2TeO_6 layer is compressed along *c*-axis (Fig. 2b). Such octahedral distortion can indicate the presence of a trigonal crystal field at Ni sites. Due to the symmetry, all the distances between the corresponding magnetic neighbors in the layer are equal (Table 2). It is very important to note (in view of the magnetic exchange interactions) that in-plane Ni-Ni distances for the second neighbor are slightly less than the Ni-Ni distances between the adjacent layers in the *c*-axis direction, and for the third neighbor they are longer. This phenomenon is specific for the sodium (and lithium) $A_2Ni_2TeO_6$ compounds due to the small size of the A-cation.

Each of magnetoactive layers is separated by layers of sodium atoms, which are in a prismatic oxygen surrounding. The important question for $A_2M_2TeO_6$ compounds is alkali metal ordering in the gap between honeycomb layers. Actually, according to our neutron diffraction data for the $Na_2Ni_2TeO_6$ it was found that while the positions of the tellurium, nickel, and oxygen ions are fully occupied there are only two crystallographic non-equivalent positions for sodium ions, which are occupied partially: 6g site with 69% occupation and 4c site with 31% occupation (Table 1). Besides, it was detected the total absence of Na ions at 2a site that brings some changes to the magnetic interaction scheme. Namely, it leads to a reduction of the possible ways for interlayer coupling that should have a significant impact on the interlayer magnetic interaction. There are two different ways of the magnetic interaction with the adjacent layers through two Na positions. For Na1, the triangular NaO_6 prism shares two edges with NiO_6 and one edge with TeO_6 octahedra from the layers above and below, while Na2-contained prisms share faces with NiO_6 octahedra on top and bottom sides of the prism (Fig. 3). Thus, the refinement of the occupation of the sodium positions (Table 1) showed that the energetically unprofitable Na3 position sandwiched between two TeO_6 octahedra is empty, and the occupations of the Na1 and Na2 sites are slightly increased.

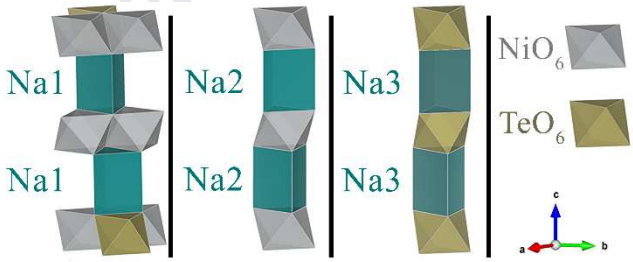

Fig. 3. Honeycomb layers possible connections through Na1, Na2 and Na3 triangle oxygen prisms.

The DFT calculations in [29] showed that, despite the strong change in Na distribution, the interlayer magnetic interactions are much smaller in comparison with the intralayer, which mainly determine the magnetic ground state realized in this system.

During Rietveld refinement, thermal parameters of two Na ions located at nonequivalent Wyckoff positions were considered as anisotropic and restricted to be the same (Table 1). Important to note that the anisotropic components showed a small value of U_{33} compared to U_{11} and U_{22}, which emphasizes the presence of significant thermal fluctuations within the sodium layer. It is quite possible that this is due to Na sites splitting and not only to the thermal oscillations anisotropy.

In addition small but noticeable due to the resolution of SSPD neutron diffractometer anisotropic peaks broadening has been observed. This indicates the presence of crystal defects in the studied sample and primarily we associate it with the stacking faults that is generally accepted for the layered systems. Since $Na_2Ni_2TeO_6$ is out of the general $A_2M_2TeO_6$ sequence with *P6₃22* space group ordering, it is natural to expect for it the presence of such phenomena due to the possible poor layer assembly.

Results of the full-profile analysis of the high-resolution synchrotron powder diffraction pattern at RT is presented in Fig. 4. In view of crystal structure complexity (and its non-ideality), Rietveld refinement becomes difficult and determination of fine details is practically impossible.

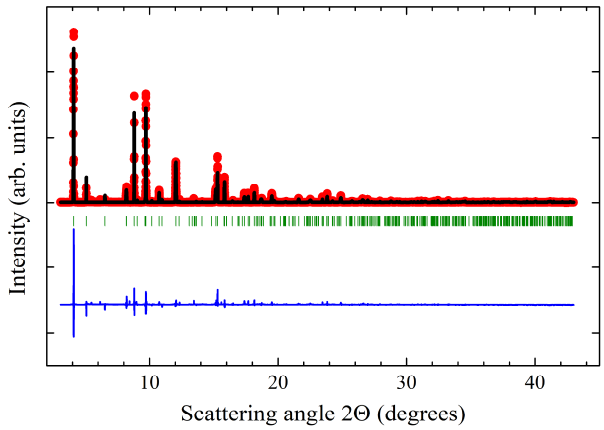

Fig. 4. RT synchrotron diffraction pattern of $Na_2Ni_2TeO_6$. Red circles are experimental data, black solid line is calculated profile, vertical bars are positions of Bragg peaks, and blue solid line is difference curve shifted down for convenience.

However, the huge broadening of the peaks with large *l* and the presence of the shoulders for the reflections series (00*l*) and (11*l*) with $l > 2$ (Fig. 5b) should be noticed. This is most likely related to the poor layers stacking, which leads to interlayer distance increasing (shoulders appear at the small angle region, that is, at large *d*-spacing near the main reflection). Another observation is a characteristic “tail” near the (100) structure reflection, on which other peaks are observed and not indexed with the *P6₃/mcm* space group (Fig. 5a).

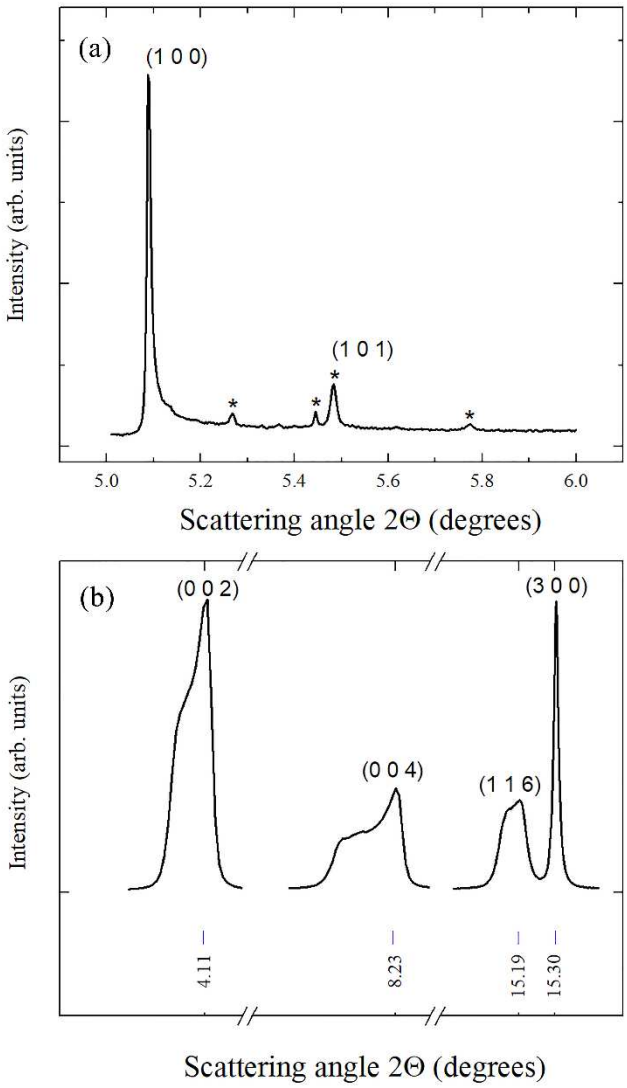

Fig. 5. RT synchrotron diffraction pattern of $Na_2Ni_2TeO_6$. a) Enlarged area near the (1 0 0) structure reflection with characteristic "tail". Asterisks marks positions of unindexed in *P6₃/mcm* space group peaks. It is marked the additional (1 0 1) reflection allowed in *P6₃22*. b) Example of broadening reflections with different *l*-indexes.

Such feature was observed for other layered compounds and was explained with stacking faults presence [33, 34]. The weak (101) and (103) reflections are visible on the synchrotron data, which is forbidden in *P6₃/mcm* space group, but are allowed in *P6₃22* that indicates the fractional presence of this polytype in the resulted crystal structure due to a failure in the layer packing. The ordering in *P6₃22* space group is formed by the layer-to-layer transition vector (2/3 1/3 0) relative to the main crystallographic axes. Thus, the new chains with Ni-Te-Ni-Te alternation are formed along the *c*-axis. Moreover, the other smaller peaks on the tail of the (100) reflection indicate the presence of the other superstructures associated with different translations of the layers relative to each other. Synchrotron data showed unambiguously that the crystal ordering of $Na_2Ni_2TeO_6$ is the result of complex packing of the honeycomb Ni_2TeO_6 layers and

sodium layers. The diffraction experiment indicated the average *P6₃/mcm* structure ordering, which is distorted by the small presence of characteristic stacking faults. Herewith, the structure of separate honeycomb magnetic layer remains unchanged what is very important in view of magnetism.

3.2 Temperature and field dependences of magnetization

Summary of the magnetization data for $Na_2Ni_2TeO_6$ at various magnetic fields is presented in Fig. 6.

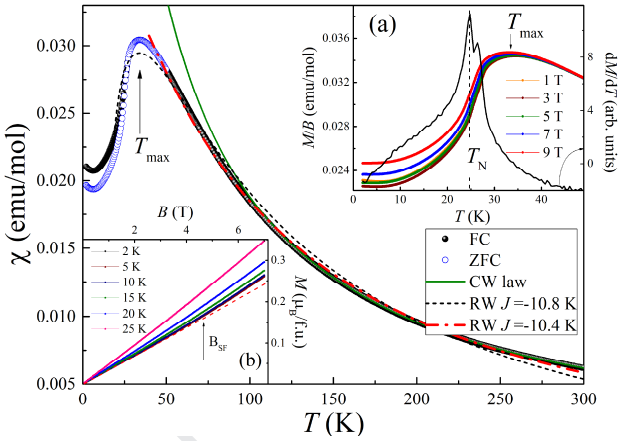

Fig. 6. Temperature dependence of magnetic susceptibility $\chi = M/B$ for $Na_2Ni_2TeO_6$ at B = 1 T. The solid green curve shows the result of the Curie-Weiss approximation. Dashed red and black curves are results of approximation according to Rushbrooke – Wood model for 2D honeycomb lattice. Insets: (a) Temperature dependence of M/B and its derivative under variation of magnetic field. (b) Magnetization isotherms at different temperatures.

With temperature decreasing the magnetic susceptibility $\chi = M/B$ passes through a relatively broad correlation maximum at T_{max} ~ 34 K, characteristic for low-dimensional systems, which is replaced by a weak kink and eventually it falls by about one third. Small discrepancy between $\chi(T)$ dependences recorded in the field-cooled (FC) and zero-field cooled (ZFC) cooling regimes confirms a good quality of the sample under study. Such a behavior is typical for polycrystalline easy-axis antiferromagnets and indicates the onset of a long-range antiferromagnetic order at low temperatures, which is preceded by short-range ordering effect on 2D honeycomb lattice. The Neel temperature may be estimated from the maximum of the $d\chi/dT$ (T) dependence and was found to be $T_N \approx 25$ K. In the high-temperature region, the behavior of $\chi(T)$ is well described by the Curie-Weiss law with the addition of a temperature-dependent term:

$$\chi = \chi_0 + \frac{C}{T - \Theta} \qquad (1)$$

where Θ is the Weiss temperature, C is the Curie constant $C = N_A \cdot \mu_{eff}^2 \cdot \mu_B^2 / 3k_B$, N_A is Avogadro's number, μ_{eff} is the effective magnetic moment, μ_B is Bohr's magneton, and k_B is Boltzmann's constant. The best fitting according to Eq. 1 in the range 150 – 300 K resulted in $\chi_0 \sim 1\times10^{-3}$ emu/mol, C = 2.37 mol K/emu and Θ = -18.5 ± 0.5 K. The negative value of the Weiss temperature indicates the predominance of antiferromagnetic exchange couplings, and its relatively small value implies the existence of strong competition between FM and AFM interactions. The effective magnetic moment determined from the corresponding Curie constant was found to be 4.35 μ_B/f.u. which is in excellent agreement with theoretical estimates $\mu_{theor}^2 = g^2\mu_B^2 nS(S+1)$, where n is number of Ni^{2+} ions per formula unit, using an effective g-value 2.19 obtained from ESR data (see below).

Structural conditions for $Na_2Ni_2TeO_6$ allow us to apply the high temperature series expansion (HTSE) model for 2D planar honeycomb lattice the analysis of the magnetic susceptibility. For 2D honeycomb lattice with the S = 1 one can use the expression of Rushbrook and Wood (RW) [35]:

$$\chi = (2Ng^2\beta^2/3kT)(1+Ax+Bx^2+Cx^3+Dx^4+Ex^5+Fx^6)^{-1} \qquad (2)$$

where $x=|J|/kT$, k = 1.3807 × 10^{-16} ergK^{-1}, N is Avogadro's number, β =9.274 × 10^{-21} erg G^{-1}, A = 4, B = 7.333, C = 7.111, D = – 5.703, E = – 22.281, and F = 51.737 [35].

It is worth to note that this Eq.2 is valid only down to a certain temperature, since it becomes not quantitative when the ratio $kT/J \rightarrow 1$, because only limited number of terms (six) were calculated [35] in the infinite series. Hence, we can approximate the temperature dependence of the magnetic susceptibility according to Eq. 2 above the maximum temperature. As one can see from Fig. 6 this approximation (dash-dotted red curve) gives a good agreement with the experimental data over the wide temperature range, which is markedly higher than the range of Curie-Weiss law validation (green solid curve). The best agreement is achieved with the value of the exchange parameter J/k = - 10.8 K. This experimental value is in very reasonable agreement with the result of DFT calculations [29].

Applied magnetic fields up to 9 T does not affect essentially on the character of temperature dependence of the magnetization (upper inset (a) in Fig. 6). The maximum of the magnetization $M(T)$ very weakly shifts towards low-temperatures with increasing magnetic field, hence one can expect that the scale of exchange interactions should be substantial.

The magnetization isotherms *M(B)* for $Na_2Ni_2TeO_6$ show neither hysteresis nor saturation in the magnetic fields up to 9 T (lower inset (b) in Fig. 6). At the same time *M(B)* curves below Neel temperature demonstrate a clear upward curvature suggesting the presence of a magnetic

field induced spin-flop type transition in the compound with the critical field B_{SF} ~ 5 T at T = 2 K. With increasing temperature the position of this anomaly slightly shifts to higher fields and eventually disappears at $T > T_N$, confirming the ordering temperature. It is also noted that within this range of the applied magnetic fields, the maximum value of magnetic moment $M \approx 0.4$ μ_B/f.u. remains noticeably lower than the theoretically expected saturation magnetic moment for Ni^{2+} ions $M_S = gS\mu_B = 4.4$ μ_B/f.u.

3.3 *Specific heat*

In order to analyze the nature of the magnetic phase transition and to evaluate the corresponding contribution to the specific heat and entropy, the similar [9] diamagnetic material $Na_2Zn_2TeO_6$ has been synthesized and measured. The specific heat data for both magnetic and diamagnetic samples in the T-range 2-50 K are shown in Fig. 7. The $C(T)$ data for $Na_2Ni_2TeO_6$ in zero magnetic field are in good agreement with the temperature dependence of the magnetic susceptibility, and demonstrate a distinct λ-shaped anomaly, which is characteristic of a 3D magnetic order (Fig. 7). Note, that the absolute value of the Néel temperature $T_N \approx 25$ K for $Na_2Ni_2TeO_6$ deduced from $C_p(T)$ data at B = 0 T perfectly coincides with maximum on the Fisher specific heat [36, 37] $d(\chi T)/dT(T)$ that is characteristic of low-dimensional antiferromagnets with strong short-range correlations (inset in Fig. 7).

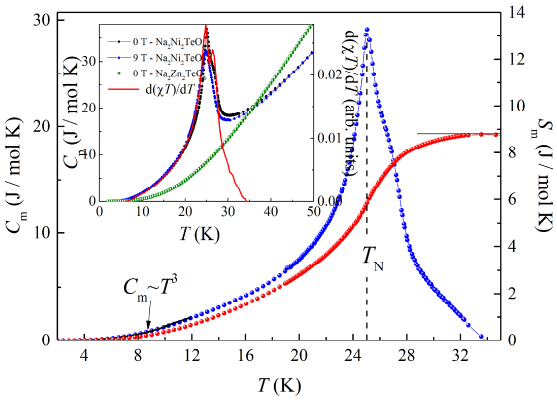

Fig. 7. Magnetic specific heat (blue circles) and magnetic entropy (red circles) for $Na_2Ni_2TeO_6$ at B = 0 T. Inset: The temperature dependences of the specific heat for $Na_2Ni_2TeO_6$ at B = 0 T (black circles), B = 9 T (blue circles) along with the data for non-magnetic analogue $Na_2Zn_2TeO_6$ (green circles) in zero magnetic field and Fisher specific heat $d(\chi T)/dT$.

We observe a specific heat jump at T_N ΔC_m ~ 30 J/mol K for $Na_2Ni_2TeO_6$, which almost reaches the value expected from the mean-field theory for the antiferromagnetic ordering of two Ni^{2+}

ions system assuming all spins to be in the high-spin (S=1) state [36]: $\Delta C_m = 5R\frac{2S(S+1)}{S^2+(S+1)^2} \approx$ 33.2 J/(mol K), where R is the gas constant R=8.31 J/mol K.

In applied magnetic fields, the T_N - anomaly only slightly shifts to lower temperatures similarly behavior of the magnetization (inset (a) in Fig. 6).

For quantitative estimations we assume that the specific heat of the isostructural compound $Na_2Zn_2TeO_6$ provides a proper estimation for the pure lattice contribution to specific heat. In the frame of the Debye model the phonon specific heat is described by the function [38]:

$$C_{ph} = 9R\left(\frac{T}{\Theta_D}\right)^3 \int_0^{\Theta_D/T} \frac{e^x x^4}{(e^x-1)^2} dx \qquad (3)$$

where $x = \hbar\omega/k_B T$, $\Theta_D = \hbar\omega_{max}/k_B$ is the Debye temperature, ω_{max} is the maximum frequency of the phonon spectrum and k_B is the Boltzmann constant. The value of the Debye temperature Θ_D estimated from approximating $C(T)$ to this T^3 – law in the low temperature range for the diamagnetic compound $Na_2Zn_2TeO_6$ was found to be about ~ 330 ± 10 K. Normalization of the Debye temperatures has been made taking into account the difference between the molar masses for Zn / Ni atoms resulting in Θ_D ~ 339 ± 10 K for $Na_2Ni_2TeO_6$. The entropy change was calculated using the equation: $\Delta S_m(T) = \int_0^T \frac{C_m(T)}{T} dT$. We observe that the magnetic entropy ΔS_m saturates at temperatures higher than 33 K with value lower than the magnetic entropy change expected from the mean-field theory $\Delta S_m(T) = 2R\ln(2S+1) \approx$ 18.3 J/(mol K). Such a behavior is frequently observed for materials with lower magnetic dimensionality and coexistence of long and short-range correlations [39, 40].

The magnetic contribution to the specific heat was determined by subtracting the lattice contribution using the data for the isostructural non-magnetic analogue (Fig. 7). At lowest temperatures we have examined the $C_m(T)$ in terms of the spin-wave (SW) approach assuming that the limiting low-temperature behavior of the magnetic specific heat should follow a $C_m \sim T^{d/n}$ - power law, where d stands for the dimensionality of the magnetic lattice and n is defined as the exponent in the dispersion relation $\omega \sim \kappa^n$ [39]. The least square fitting of the data below T_N agrees well with d = 3 and n = 1, that corroborates the picture of 3D AFM magnons at low temperatures.

3.4 ESR spectroscopy

In the paramagnetic phase ($T > T_N$), a single broad Lorentz type line is observed in the ESR absorption spectra (Fig. 8), apparently corresponding to the signal from Ni^{2+} ions. The main

ESR parameters (effective g-factor, the ESR linewidth and the integral ESR intensity) were deduced by fitting the experimental spectra with Lorentzian profile taking into account two circular components of the exciting linearly polarized microwave field on both sides of $B = 0$,

$$\frac{dP}{dB} \propto \frac{d}{dB}\left[\frac{\Delta B}{\Delta B^2 + \left(B - B_r\right)^2} + \frac{\Delta B}{\Delta B^2 + \left(B + B_r\right)^2}\right] \quad (4)$$

where P is the power absorbed in the ESR experiment, B is the magnetic field, B_r is the resonance field, and ΔB is the linewidth.

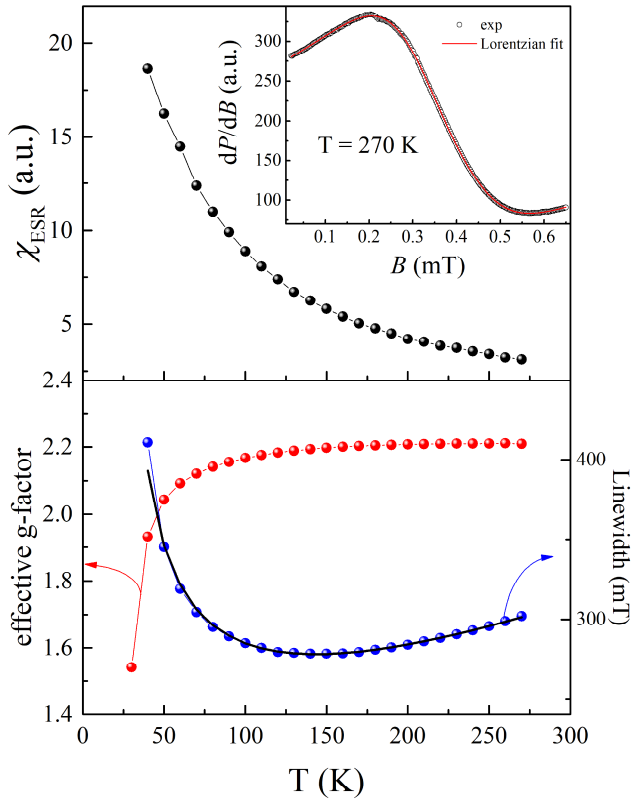

Fig. 8. Temperature dependences of the integral ESR intensity (upper panel) as well as effective g-factor and ESR linewidth (lower panel) for $Na_2Ni_2TeO_6$. The black solid curve on lower panel represent the result of fitting in the frame of modified Huber theory as described in the text. On inset the representative example of ESR absorption spectrum (circles) at room temperature and its fitting by Lorenzian profile (red curve).

At high temperatures, the ESR line is characterized by an isotropic temperature-independent effective g-factor, which is approximately g = 2.19 ± 0.02. When cooling the sample below T ~120 K, the g- value factor to be temperature-independent and there is a noticeable shift of the resonant field towards smaller magnetic fields.

The integral intensity of the ESR spectra χ_{esr}, which is proportional to the number of magnetic spins, was estimated using double integration of the first derivative of the experimental

absorption line for each temperature. In the paramagnetic phase it demonstrates Curie-Weiss type behavior in a good agreement with the static magnetic susceptibility.

The linewidth decreases weakly and almost linearly upon lowering of the temperature, passes through minimum at ~ 140 K and eventually changes the trend. Upon further decrease of the temperature the absorption line broadens significantly and the ESR signal vanishes in the vicinity of the Néel temperature, indicating an opening of an energy gap for resonance excitations, e.g., due to the establishment of AFM order. The broadening of the ESR line may be treated in terms of critical behavior of ESR linewidth due to slowing down of spin fluctuations in the vicinity of an order-disorder transition [41-44]. To account for the ΔB behavior over the whole temperature range we have also included the linear term $D \cdot T$ into the fitting formula:

$$\Delta B(T) = \Delta B^{*} + A \cdot \left[\frac{T_N^{ESR}}{T - T_N^{ESR}} \right]^{\beta} + D \cdot T \qquad (5)$$

where the first term ΔB^{*} describes the high-temperature limit of the width of the exchange-constricted line, and the second term is responsible for the critical behavior when approaching the temperature of ordering $T^{ESR}{}_N$ from above, A is an empirical parameter and β is a critical exponent.

It is found that the theoretical dependence satisfactorily describes the experimental data in a wide temperature range above the Neel temperature. The best agreement by the least squares method was obtained with the values of the following parameters ΔB^{*} = 177 ± 3 mT, A = 200 ± 3 mT, D = 3.4, $T^{ESR}{}_N$ = 20 ± 2 K and β = 0.75 ± 0.05. The value of the critical exponent is noticeably larger than the expected β = 1/3 for the 3D Heisenberg antiferromagnet in the frame of Kawasaki approach [42, 43] and probably indicates rather 2D character of exchange interactions in $Na_2Ni_2TeO_6$ in accordance with layered quasi-2D network of magnetic sublattice. For example, such values were observed earlier for other 2D antimonates of alkali and nickel, such as β ~ 0.9 for 2D $Li(Na)_3Ni_2SbO_6$ [45].

3.5 Magnetic Phase Diagram

Summarizing the thermodynamic data on the field and temperature dependences of the magnetization, as well as specific heat, we can construct a magnetic phase diagram for the $Na_2Ni_2TeO_6$ tellurate (Fig. 9). The ground state is antiferromagnetic, but it is complicated by presence of field-induced spin-flop phase. A transition from the paramagnetic to the antiferromagnetic phase takes place at 25 K, but prior this a strong short-range ordering effect is observed. As the magnitude of the magnetic field increases, the phase boundary shifts weakly towards lower temperatures. The estimated magnetic moment of saturation for two Ni^{2+} ions (S =

1) in $Na_2Ni_2TeO_6$ is $M_S \approx 4.4$ μ_B/f.u. which is significantly higher than the maximum value reached $M \approx 0.4$ μ_B/f.u. in the investigated range of magnetic fields. The expected saturation field of magnetization is ~ 85 T, which greatly exceeds the range of the fields studied (up to 9 T).

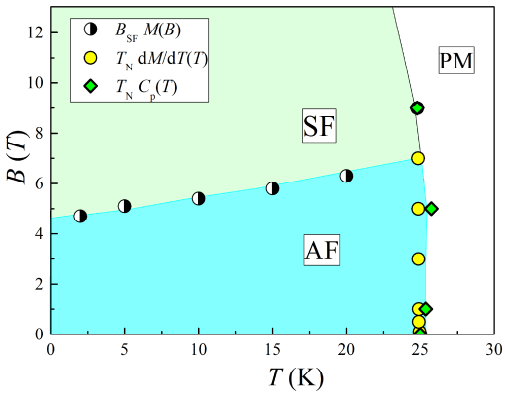

Fig. 9. Magnetic phase diagram of $Na_2Ni_2TeO_6$

3.6 Magnetic structure

Experimental low-temperature neutron measurements data from G4.1 diffractometer are presented in Fig. 10. It is important to note that the previous work of Karna et al. [29] has already reported signatures of both strong incommensurate (ICM) and weak commensurate antiferromagnetic spin ordering in $Na_2Ni_2TeO_6$ by means magnetic neutron diffraction, but no relevant Rietveld refinement had been carried out. Their neutron data demonstrate a broadened single peak that was indexed with incommensurate in all directions propagation vector k = (0.47 0.44 0.28). In contrast, our sample shows a pure single-phase ordering corresponding to an antiferromagnetic magnetic structure with the same propagation vector as in [29] for commensurate peaks, which will be shown later. The important question of whether this incommensurability is a result of sample preparation features or helical magnetic ordering requires additional research.

However, for other honeycomb compounds, a commensurate spin structure with a single propagation vector is usually observed, which, in particular, was obtained for the isostructural $Na_2Co_2TeO_6$ compound [46].

The appearance of additional reflections within the low diffraction angles especially within the angles lower than the angular position of the first (002) crystallographic reflection uniquely indicates the antiferromagnetic spin ordering nature, which agrees well with the macromagnetic properties. Magnetic peaks have a slightly asymmetric shape with typical Lorentzian tails.

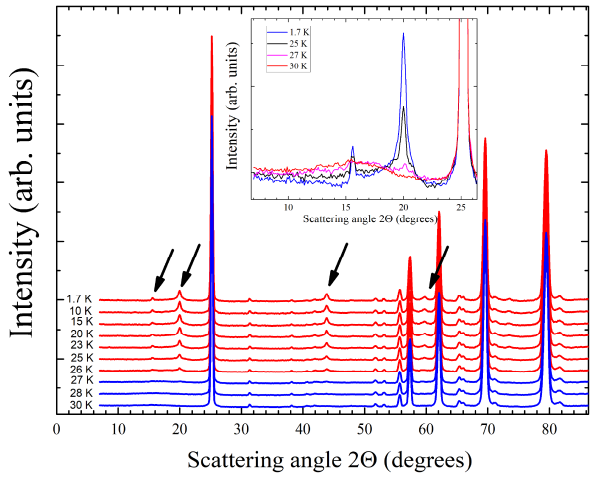

Fig. 10. Low temperature neutron diffraction patterns of $Na_2Ni_2TeO_6$ (G4.1, λ = 2.422Å). Arrows are pointing at the most intense additional reflections associated with magnetic scattering appearing at temperatures lower than 27 K. Inset: Low angle part of diffraction patterns with the neutron diffuse scattering.

At 2θ = 16° (in the area of (0 0 0) + *k* magnetic reflection) the diffuse magnetic scattering can be observed on neutron diffraction patterns at 25, 26, 27, 28, 30 K, which is most likely related to the presence of the short-range magnetic correlations in compound (inset in Fig. 10). Such behavior has been noticed earlier on similar compounds $Na_2Co_2TeO_6$ [46] and $BaNi_2V_2O_8$ [47]. Besides, there are some additional low-intensity Bragg peaks from the uncertain phase(s), which have not been described in our model (see Crystal Structure). The behavior of these peaks remain unchanged in the temperature range from 1.7 K to 30 K, therefore the presence of impurity does not prevent us in analysis of magnetic Bragg scattering.

In order to determine the magnetic structure without any influence of the impurity peaks, we use the difference pattern between the patterns measured at 1.7 and 30 K (Fig. 11). The up-down features of the difference pattern appearing at 2θ = 24.2° and 2θ = 69.5° are created by the slight thermal expansion between 1.7 K and 30 K which leads to an incomplete subtraction of the most intensive (002) and (113) nuclear reflections.

It is remarkable that there are three equivalent solutions for magnetic structure in view of the group-theoretical analysis based on the symmetry of hexagonal crystal structure. All magnetic peaks can be indexed with the propagation vectors k_1 = (1/2 0 0), k_2 = (0 1/2 0) or k_3 = (1/2 1/2 0). They correspond to an antiferromagnetic arrangement with a magnetic cell doubled along *a*-axis, along *b*-axis or along both *a*- and *b*-axis respectively, according to the crystal unit cell of the $Na_2Ni_2TeO_6$.

The unit cell contains four nonequivalent nickel atoms at the 4d site, which occupy the positions specified in Table 3.

Table 3. Basis vectors of Γ_4 irreducible representation for propagation vector k = (1/2 0 0) and *P6₃/mcm* space group. The symmetry operators correspond to four nonequivalent Ni positions within the unit cell: Ni1: (1/3, 2/3, 0); Ni2: (2/3, 1/3, 1/2); Ni3: (2/3, 1/3, 0); Ni4: (1/3, 2/3, 1/2)

IR		Basis Vectors			
	Symm:	x,y,z	-x+1,-y+1,z+1/2	-x+1,-y+1,-z	x,y,-z+1/2
Γ_4	Ψ_1	(0 -1 0)	(0 -1 0)	(0 -1 0)	(0 -1 0)
	Ψ_2	(0 0 1)	(0 0 -1)	(0 0 1)	(0 0 -1)

Their magnetic moment components related to each other by the symmetry operators, which impose constraints to magnetic moments directions and their magnitudes. The representational analysis based on the propagation vector k_1= (1/2 0 0) and the crystallographic space group *P6₃/mcm* yields to 8 one dimensional magnetic irreducible representations (IR), four of them appearing once and another four appearing twice. The magnetic representation Γ_{mag} is could be composed of eight IRs as

$$\Gamma_{mag} = \Gamma_1^1 + \Gamma_2^1 + 2\Gamma_3^1 + 2\Gamma_4^1 + 2\Gamma_5^1 + 2\Gamma_6^1 + \Gamma_7^1 + \Gamma_8^1.$$

The basis vectors are calculated using the projection operator technique implemented in the BASIREPS program, included in the FullProf suite. Each of Γ_1, Γ_2, Γ_7, and Γ_8 has one basis vector, whereas Γ_3, Γ_4, Γ_5, Γ_6 have two basis vectors. The low temperature long-range magnetic structure was solved through Rietveld refinement by including basis vector and symmetry information in the pcr-file. Possible IRs were tested by refining the pure magnetic powder diffraction pattern using the scale factor and the peak shape parameters determined from the high temperature structure refinement. The best fitting was obtained considering the magnetic structure associated with the Γ_4 irreducible representation. The basis vectors of this representation (the Fourier components of the magnetization) are given in Table 3. The refined pure magnetic diffraction pattern (without nuclear contribution) at 1.7 K is shown in Fig. 11.

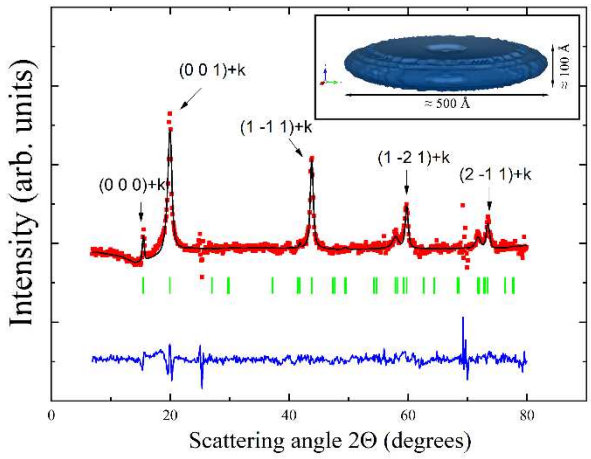

Fig. 11. The refined magnetic diffraction pattern of $Na_2Ni_2TeO_6$ without nuclear contribution at 1.7 K. (G4.1, λ = 2.422 Å). The vertical bars indicate positions of magnetic Bragg peaks. The most intensive magnetic reflections are pointed out by arrows and indexes. k = (1/2 0 0), χ^2 = 2.72, R_f = 1.81 %. Inset: visualization of the average coherent magnetic scattering region.

The resulting magnetic structure is shown in Fig. 12. Two free parameters associated with the presence of two basis vectors for Γ_4 irreducible representation allow to vary the magnetic moments magnitudes along *b*- and *c*- directions independently. The best fitting was reached when the magnetic moment of nickel atoms preferably directed along the *c*-axis with component equal to M_c = 1.67(1) μ_B and with inclination along the *b*-axis represented by nonzero component equal to M_b = 0.41(1) μ_B, which about 24% of the M_c. The refined total magnetic moment value obtained to be M = 1.72(1) μ_B/Ni. The problem of the presence or absence of the magnetic moment inclination, which has already been noted earlier in study of the related $Na_2Co_2TeO_6$ compound [48], but which has not received sufficient attention, is actually quite important. Without taking into account the M_b, the resulting magnetic structure can be considered as zigzag ferromagnetic chains coupled antiferromagnetically in *ab*-plane (Fig. 12a) and the interlayer interactions along *c*-direction are antiferromagnetic. The presence of *b*-component leads to a slight ferromagnetic interaction along the *c*-direction according to symmetry of Γ_4 irreducible representation (Fig. 12b).

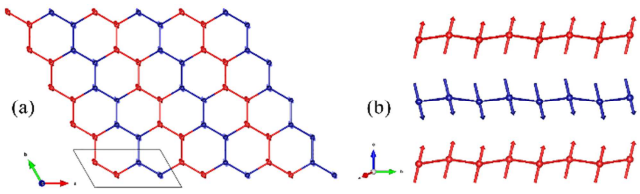

Fig. 12. The magnetic structure of $Na_2Ni_2TeO_6$ at 1.7 K. Different colors denote opposite spin directions. a) Zigzag magnetic order in honeycomb layer. b) Representation of zigzags in adjacent layers.

As noted earlier, the crystal structure symmetry leads to three different solutions for propagation vectors k_1= (1/2 0 0), k_2= (0 1/2 0) or k_3= (1/2 1/2 0). The low-temperature neutron diffraction data treatment showed that all propagation vectors correspond to the same zigzag magnetic structure, but the direction of zigzag chains is different. They are pointed along the [0 1 0], [1 0 0] and [1 1 0] crystallographic directions for k_1, k_2 and k_3, respectively. To avoid such ambiguity we use the Shubnikov magnetic group approach, which is implemented in Fullprof suite. It was found that all magnetic structure solutions correspond to the magnetic space group C_Pmcm' (#63.13.523) in the OG notation [49].

Zigzag magnetic order means that three of six successive spins from the honeycomb block are parallel and the other three are antiparallel to them. In other words, each spin on honeycomb net has two ferromagnetically coupled nearest neighbors and one antiferromagnetically coupled, and for the second neighbors, the antiferromagnetic couplings are dominant and so on. Thus, this magnetic order is a result of strong intralayer interactions competition on the honeycomb net. In this system, Ni ions are separated by ligands, so that the direct exchange between magnetic atoms *d*-orbitals is difficult and hopping processes occur via ligand *p*-orbitals. As was recently described in the review [50] in the case when two neighboring MO_6 octahedra share their edges there will also be a 90° superexchange interaction: first of all, a moderate AFM exchange appears via the same *p*-orbital of oxygen; second, there is also a possible FM superexchange between two half-filled e_g- (or t_{2g}-) orbitals via two different *p*-orbitals. The exchange processes with further neighbors can be realized via not only one but several intermediate ions (two oxygen and tellurium in case of the second neighbor) that is the known as super-super exchange [51, 52]. Furthermore, the distance between adjacent layers is comparable to the distances between different neighbors in one layer but the magnetic interaction travels a more complex path (through an alkali metal and two oxygen atoms), and the magnetic interaction is usually weaker than the others with the neighbors in the layer [29, 45].

The zigzag magnetic ground state was repeatedly observed earlier and it is probably preferable for systems with a honeycomb-like geometry, however, there are significant differences that strongly depend on the internal structure (crystallographic symmetry, distances, bond angles, etc.) and chemical composition of the compounds. For example, the zigzag magnetic order was recently found for the related $Na_2Co_2TeO_6$ compound, which has the identical honeycomb ordering to $Na_2Ni_2TeO_6$, but another layer packing in the frame of $P6_322$

space group. Both compounds demonstrate similar temperature dependences of the magnetic susceptibility, the Neel and Weiss temperatures take close values. However, the Co magnetic moments are pointed out along the *b*-axis (i.e. along zigzag precisely) and lies completely in the honeycomb plane as opposite to the Ni magnetic moments, which are almost perpendicular to layers. Such anisotropy in magnetic moment directions was also observed for compounds with monoclinic crystal structure $Cu_3M_2SbO_6$ (M = Co, Ni) [53].

Then we should talk about the value of the magnetic moment. Since $3d^8$ Ni^{2+} with e_g-t_{2g} splitting by an octahedral crystal field should have the electron configuration as $e^2_g t^6_{2g}$ for S = 1 high-spin state, μ_{theor} = 2.7 μ_B/Ni is expected (assuming g=2.19) from spin-only contribution. The magnitude of the ordered magnetic moment derived from the neutron diffraction data at 1.7 K is smaller than the theoretically expected value. The reduced value is usually associated with both thermal fluctuations presence and the magnetic exchange frustrations between nearest and further neighbors, which are significant for such system. On the other hand, it may be associated with stacking faults in $Na_2Ni_2TeO_6$. As a result, nonideal layer arrangement diminishes magnetic peaks intensities so the value of a moment is lower than expected. Such effect was observed earlier in $Cu_3Ni_2SbO_6$ and $Cu_3Co_2SbO_6$ [53] and in $Na_2Co_2TeO_6$ [46, 48].

Besides, the behavior of the magnetic structure with the temperature was studied. For the neutron diffraction patterns measured at different temperatures T < 30 K were processed. Temperature dependence of the total magnetic moment magnitude and its components along *b*- and *c*-axis are shown in Fig. 13. This result demonstrates that increasing of temperature from 1.7 to T_N leads only to a conventional change of magnetic moment value (its decrease), but the direction of the moment remains unchanged (an angle with *c*-axis is equal to (12.7±0.5)°). It turns out that the invariance of the direction of the magnetic moment in the magnetically ordered state for the family of layered oxides with honeycomb superstructure of a layer of the $A_2M_2TeO_6$ type differs from the case of related $A_3M_2SbO_6$ oxides, where the phenomenon of turn of the magnetic moment with decreasing temperature from the direction along the *c*-axis to a direction perpendicular to the honeycomb plane was revealed, for example on $Li_3Ni_2SbO_6$ [54]. This difference can be explained by the monoclinic crystal structure of $A_3M_2SbO_6$.

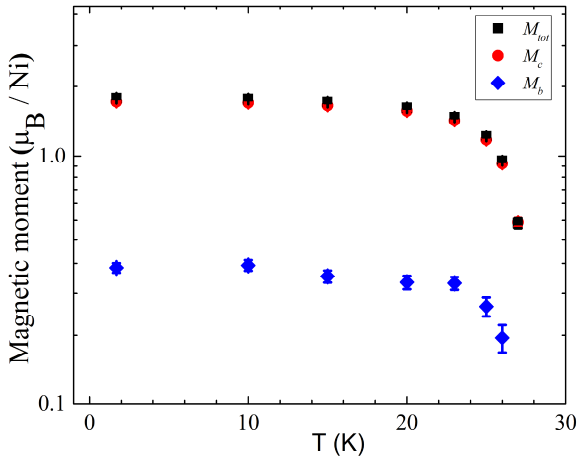

Fig. 13. Temperature dependence of the magnetic moment magnitude and its components along *b*- and *c*-axis (logarithmic scale).

Due to the difference in the magnetic peaks form and especially broadening in comparison with nuclear reflections, their widths were simulated using the size formalism presented in the FullProf suite. The size effect (simulating the direction dependence of the magnetic correlations) was fitted using the anisotropic size-broadening model, which is implemented in the FullProf suite. As it turned out, the coherent magnetic scattering area has a disk shape that is homogeneous over the *ab* plane and compressed along the *c*-axis (inset in Fig. 11). This behavior indicates the two-dimensional nature of magnetic correlations when the correlation length along the *c*-axis is relatively small and covers about ten unit cells, while the correlation in the honeycomb plane is uniform and sizable. As a result, the broad peak on the magnetic susceptibility curve near 30K relates with 2D AFM short-range order, i.e., the interlayer correlation length must develop long enough to reach the 3D long-range order below 30 K. The neutron diffraction data show the presence of broad diffuse magnetic halo slightly above the Neel temperature, which then with the temperature decreasing develops into magnetic reflections of the fully ordered phase.

4. Conclusions

We have investigated the crystal structure of $Na_2Ni_2TeO_6$ using a combination of high-resolution synchrotron and neutron powder diffraction. The effect of stacking faults on the crystal structure is not negligible and requires careful examination.

The thermodynamic and resonance properties were received by temperature and field dependences of magnetization, specific heat, and ESR measurements. The onset of long-range magnetic order was found about T_N = 25±1 K, which is preceded by a short-range order on 2D

honeycomb lattice. Detailed study of the magnetic properties in wide range of temperature and applied magnetic fields was performed, which allowed to construct the magnetic phase diagram. For the first time we have revealed field-induced spin-reorientation transition on the magnetization isotherms. Spin-dynamics from helium to room temperature was studied and in particular was determined the temperature behavior of ESR linewidth which is proportional to spin-correlation length and it is quite unusual for honeycomb 2D Ni-based compounds.

The ground magnetic state of $Na_2Ni_2TeO_6$ below T_N has been determined using low-temperature neutron diffraction. It represents a commensurate antiferromagnetic zigzag-type structure with the spins that are almost perpendicular to the honeycomb layers. The diffuse magnetic neutron scattering above T_N related with the strong short-range spin-spin correlations presence was found. We cleared up the coexistence of the short and long-range order in this quasi- 2D compound and these observations give much more self-consistent picture taking into account structural conditions and organization of the spin-configuration. The coherent magnetic scattering area has a disk shape that is homogeneous over the *ab* plane and compressed along the *c*-axis that indicates 2D nature of magnetic correlations in the compound. Restricted along c-axis coherent scattering area and the ESR measurements indicate the quasi-two-dimensional nature of the compound.

Acknowledgment

The reported study was funded by Russian Science Foundation according to the research projects № 18-12-00375 (A.I.K., S.Yu.P and A.N.K.) and by Russian Foundation for Basic Research through grant 18-02-00326 (E.A.Z., S.M.I. and R.G.V.). The authors thank V.B. Nalbandyan, Chemistry Faculty, Southern Federal University, Rostov-on-Don, for providing the $Na_2Ni_2TeO_6$ sample for the study.

References

[1] J. Xu, A. Assoud, N. Soheilnia, S. Derakhshan, H.L. Cuthbert, J.E. Greedan, M.H. Whangbo, H. Kleinke, Synthesis, Structure, and Magnetic Properties of the Layered Copper(II) Oxide $Na_2Cu_2TeO_6$, Inorg. Chem. 44 (2005) 5042-6. https://doi.org/10.1021/ic0502832.

[2] L. Viciu, Q. Huang, E. Morosan, H.W. Zandbergen, N.I. Greenbaum, T. McQueen, R.J. Cava, Structure and basic magnetic properties of the honeycomb lattice compounds $Na_2Co_2TeO_6$ and $Na_3Co_2SbO_6$, J. Solid State Chem. 180 (2007) 1060-1067. https://doi.org/10.1016/j.jssc.2007.01.002.

[3] V.V. Politaev, V.B. Nalbandyan, A.A. Petrenko, I.L. Shukaev, V.A. Volotchaev, B.S. Medvedev, Mixed oxides of sodium, antimony (5+) and divalent metals (Ni, Co, Zn or Mg), J. Solid State Chem. 183 (2010) 684-691.

https://doi.org/10.1016/j.jssc.2009.12.002.

[4] E.A. Zvereva, M.A. Evstigneeva, V.B. Nalbandyan, O.A. Savelieva, S.A. Ibragimov, O.S. Volkova, L.I. Medvedeva, A.N. Vasiliev, R. Klingeler, B. Büchner, Monoclinic honeycomb-layered compound $Li_3Ni_2SbO_6$: Preparation, crystal structure and magnetic properties, Dalton Trans. 41 (2012) 572-580. https://doi.org/10.1039/C1DT11322D.

[5] R. Berthelot, W. Schmidt, A. W. Sleight, M.A. Subramanian, Studies on solid solutions based on layered honeycomb-ordered phases P2-$Na_2M_2TeO_6$ (M=Co, Ni, Zn), J. Solid State Chem. 196 (2012) 225-231. https://doi.org/10.1016/j.jssc.2012.06.022.

[6] R. Berthelot, W. Schmidt, S. Muir, J. Eilertsen, L. Etienne, A.W. Sleight, M.A. Subramanian, New Layered Compounds with Honeycomb Ordering: $Li_3Ni_2BiO_6$, $Li_3NiM'BiO_6$ (M′ = Mg, Cu, Zn), and the Delafossite $Ag_3Ni_2BiO_6$, Inorg. Chem. 51 (2012) 5377-5385. https://doi.org/10.1021/ic300351t.

[7] W. Schmidt, R. Berthelot, A.W. Sleight, M.A. Subramanian, Solid solution studies of layered honeycomb-ordered phases O3–$Na_3M_2SbO_6$ (M=Cu, Mg, Ni, Zn), J. Solid State Chem. 201 (2013) 178-185. https://doi.org/10.1016/j.jssc.2013.02.035.

[8] E.M. Seibel, J.H. Roudebush, H.Wu, Q. Huang, M.N. Ali, H. Ji, R.J. Cava, Structure and Magnetic Properties of the α-$NaFeO_2$-Type Honeycomb Compound $Na_3Ni_2BiO_6$, Inorg. Chem. 52 (2013) 13605-13611. https://doi.org/10.1021/ic402131e.

[9] M.A. Evstigneeva, V.B. Nalbandyan, A.A. Petrenko, B.S. Medvedev, A.A. Kataev, A new family of fast sodium ion conductors: $Na_2M_2TeO_6$ (M= Ni, Co, Zn, Mg), Chem. Mater. 23 (2011) 1174-1181. https://doi.org/10.1021/cm102629g.

[10] A. Gupta, C.B. Mullins, J.B. Goodenough, $Na_2Ni_2TeO_6$: evaluation as a cathode for sodium battery, Power Sources 243 (2013) 817-821. https://doi.org/10.1016/j.jpowsour.2013.06.073.

[11] K. Sau, P.P. Kumar, Role of ion–ion correlations on fast ion transport: molecular dynamics simulation of $Na_2Ni_2TeO_6$, J. Phys. Chem. C 119 (2015) 18030-18037. http://dx.doi.org/10.1021/acs.jpcc.5b04087.

[12] J.B. Fouet, P. Sindzingre, C. Lhuillier, An investigation of the quantum J_1-J_2-J_3 model on the honeycomb lattice, Eur. Phys. J. B 20 (2001) 241-254. https://doi.org/10.1007/s100510170273.

[13] P.H.Y. Li, R.F. Bishop, D.J.J. Farnell, C.E. Campbell, Phase Diagram of the J_1, J_2, J_3 Heisenberg Models on the Honeycomb Lattice: A Series Expansion Study, Phys. Rev. B 86 (2012) 144404. https://doi.org/10.1103/PhysRevB.86.144404.

[14] P.H.Y. Li, R.F. Bishop, Ground-state phases of the spin-1 J_1-J_2 Heisenberg antiferromagnet on the honeycomb lattice, Phys. Rev. B 93 (2016) 214438. https://doi.org/10.1103/PhysRevB.93.214438

[15] Kitaev, Anyons in an exactly solved model and beyond, Ann. Phys. 321 (2006) 2-111. https://doi.org/10.1016/j.aop.2005.10.005.

[16] H.S. Kim, A. Catuneanu, H.Y. Kee, Kitaev magnetism in honeycomb $RuCl_3$ with intermediate spin-orbit coupling, Phys. Rev. B 91 (2015) 241110(R). https://doi.org/10.1103/PhysRevB.91.241110 .

[17] J. Chaloupka, G. Jackeli, G. Khaliullin, Kitaev-Heisenberg model on a honeycomb lattice: possible exotic phases in iridium oxides A_2IrO_3. Phys. Rev. Lett. 105 (2010) 027204. https://doi.org/10.1103/PhysRevLett.105.027204.

[18] R.D. Johnson, S.C. Williams, A.A. Haghighirad, J. Singleton, V. Zapf, P. Manuel, I. I. Mazin, Y. Li, H.O. Jeschke, R. Valentí, and R. Coldea. Monoclinic crystal structure of $\alpha-RuCl_3$ and the zigzag antiferromagnetic ground state, Phys. Rev. B. 92 (2015) 235119. https://doi.org/10.1103/PhysRevB.92.235119.

[19] Y. Singh, S. Manni, J. Reuther, T. Berlijn, R. Thomale, W. Ku, S. Trebst, P. Gegenwart, Relevance of the Heisenberg-Kitaev model for the honeycomb lattice iridates A_2IrO_3, Phys. Rev. Lett. 108 (2012) 127203. https://doi.org/10.1103/PhysRevLett.108.127203.

[20] X. Liu, T. Berlijn, W.-G. Yin, W. Ku, A. Tsvelik, Y.-J. Kim, H. Gretarsson, Y. Singh, P. Gegenwart, J.P. Hill, Long-range magnetic ordering in Na_2IrO_3, Phys. Rev. B 83 (2011) 220403. https://doi.org/10.1103/PhysRevB.83.220403.

[21] F. Ye, S. Chi, H. Cao, B.C. Chakoumakos, J.A. Fernandez-Baca, R. Custelcean, T.F. Qi, O.B. Korneta, G. Cao, Direct evidence of a zigzag spin-chain structure in the honeycomb lattice: A neutron and x-ray diffraction investigation of single-crystal Na_2IrO_3 Phys. Rev. B 85 (2012) 180403. https://doi.org/10.1103/PhysRevB.85.180403.

[22] J. Chaloupka, G. Jackeli, G. Khaliullin, Zigzag Magnetic Order in the Iridium Oxide Na_2IrO_3, Phys. Rev. Lett. 110 (2013) 097204. https://doi.org/10.1103/PhysRevLett.110.097204.

[23] K. Foyevtsova, H.O. Jeschke, I.I. Mazin, D.I. Khomskii, R. Valentí, Ab initio analysis of the tight-binding parameters and magnetic interactions in Na_2IrO_3, Phys. Rev. B 88 (2013) 035107. https://doi.org/10.1103/PhysRevB.88.035107.

[24] S.M. Winter, A.A. Tsirlin, M. Daghofer, J. van den Brink, Y. Singh, P. Gegenwart, R. Valenti, Models and materials for generalized Kitaev magnetism, J. Phys. Condens. Matter 29 (2017) 493002. https://doi.org/10.1088/1361-648X/aa8cf5.

[25] H. Liu, G. Khaliullin, Pseudospin exchange interactions in d7 cobalt compounds: Possible realization of the Kitaev model, Phys. Rev. B 97 (2018) 014407. https://doi.org/10.1103/PhysRevB.97.014408.

[26] R. Sano, Y. Kato, Y. Motome, Kitaev-Heisenberg Hamiltonian for high-spin d7 Mott insulators, Phys. Rev. B 97 (2018) 014408. https://doi.org/10.1103/PhysRevB.97.014408.

[27] P.P. Stavropoulos, D. Pereira, H.-Y. Kee, Microscopic mechanism for higher-spin Kitaev model, arXiv:1903.00011.

[28] R. Sankar, I.P. Muthuselvam, G. Shu, W. Chen, S.K. Karna, R. Jayavel, F. Chou, Crystal growth and magnetic ordering of $Na_2Ni_2TeO_6$ with honeycomb layers and $Na_2Cu_2TeO_6$ with Cu spin dimers, CrystEngComm 16 (2014) 10791-10796. https://doi.org/10.1039/C4CE01382D.

[29] S.K. Karna, Y. Zhao, R. Sankar, M. Avdeev, P.C. Tseng, C.W. Wang, G.J. Shu, K. Matan, G.Y. Guo, F.C. Chou, Sodium layer chiral distribution and spin structure of $Na_2Ni_2TeO_6$ with a Ni honeycomb lattice, Phys. Rev. B 95 (2017) 104408. https://doi.org/10.1103/PhysRevB.95.104408.

[30] J. Rodríguez-Carvajal, Recent advances in magnetic structure determination by neutron powder diffraction, Physica B 192 (1993) 55-69. https://doi.org/10.1016/0921-4526(93)90108-I.

[31] FullProf_suite. http://www.ill.eu/sites/fullprof/.

[32] R.D. Shannon, Revised effective ionic radii and systematic studies of interatomic distances in halides and chalcogenides, Acta Crystallogr. Sect A 32 (1976) 751-767. https://doi.org/10.1107/s0567739476001551.

[33] S.K. Choi, R. Coldea, A.N. Kolmogorov, T. Lancaster, I.I. Mazin, S.J. Blundell, P.G. Radaelli, Y. Singh, P. Gegenwart, K.R. Choi, S.-W. Cheong, P.J. Baker, C. Stock, J. Taylor, Spin waves and revised crystal structure of honeycomb iridate Na_2IrO_3, Phys. Rev. Lett. 108 (2012) 127204. https://doi.org/10.1103/PhysRevLett.108.127204

[34] J. Liu, L. Yin, L. Wu, J. Bai, S.M. Bak, X. Yu, Y. Zhu, X.Q. Yang, P.G. Khalifah, Quantification of honeycomb number-type stacking faults: application to $Na_3Ni_2BiO_6$ cathodes for Na-ion batteries, Inorg. Chem. 55 (2016) 8478-8492. https://doi.org/10.1021/acs.inorgchem.6b01078.

[35] G.S. Rushbrook, P.J. Wood, On the Curie points and high temperature susceptibilities of Heisenberg model ferromagnetics, Mol. Phys. 1 (1958) 257-283. https://doi.org/10.1080/00268975800100321.

[36] M.E. Fisher, Lattice statistics in a magnetic field, I. A two-dimensional super-exchange antiferromagnets, Proc. Roy. Soc. (London) A 254 (1960) 66. https://doi.org/10.1098/rspa.1960.0005.

[37] M.E. Fisher, Relation between the specific heat and susceptibility of an antiferromagnets, Phil. Mag. 7 (1962) 1731-1743. https://doi.org/10.1080/14786436208213705.

[38] Tari, The Specific Heat of Matter at Low Temperature, Imperial College Press (London), 2003.

[39] L.J. de Jongh, A.R. Miedema, Experiments on simple magnetic model systems, Adv. Phys., 23 (1974) 1-260. https://doi.org/10.1080/00018739700101558.

[40] R.L. Carlin, Magnetochemistry, Springer-Verlag, Berlin Heidelberg New York Tokyo, 1986.

[41] H. Mori, K. Kawasaki, Antiferromagnetic resonance absorption, Progr. Theor. Phys. 28 (1962) 971-987. https://doi.org/10.1143/PTP.28.971.

[42] K. Kawasaki, Anomalous spin relaxation near the magnetic transition, Prog. Theor. Phys. 39 (1968) 285-311. https://doi.org/10.1143/PTP.39.285.

[43] K. Kawasaki, Ultrasonic attenuation and ESR linewidth near magnetic critical points, Phys. Lett. 26A (1968) 543. https://doi.org/10.1016/0375-9601(68)90536-7.

[44] D.L. Huber, Critical-point anomalies in the electron-paramagnetic-resonance linewidth and in the zero-field relaxation time of antiferromagnets, Phys. Rev. B 6 (1972) 3180. https://doi.org/10.1103/PhysRevB.6.3180.

[45] E.A. Zvereva, M.I. Stratan, Y.A.Ovchenkov, V.B. Nalbandyan, J.-Y. Lin, E.L. Vavilova, M.F. Iakovleva, M. Abdel-Hafiez, A.V. Silhanek, X.-J. Chen, A. Stroppa, S. Picozzi, H.O. Jeschke, R. Valentí, A.N. Vasiliev, Zigzag antiferromagnetic quantum ground state in monoclinic honeycomb lattice antimonates $A_3Ni_2SbO_6$ (A = Li, Na), Phys. Rev. B 144401 (2015) 92. https://doi.org/10.1103/PhysRevB.92.144401.

[46] A.K. Bera, S.M. Yusuf, A. Kumar, C. Ritter, Zigzag antiferromagnetic ground state with anisotropic correlation lengths in the quasi-two-dimensional honeycomb lattice compound $Na_2Co_2TeO_6$, Phys. Rev. B 95 (2017) 094424. https://doi.org/10.1103/PhysRevB.95.094424.

[47] N. Rogado, Q. Huang, J.W. Lynn, A.P. Ramirez, D. Huse, R.J. Cava, $BaNi_2V_2O_8$: A two-dimensional honeycomb antiferromagnets, Phys. Rev. B, 65 (2002) 144443. https://doi.org/10.1103/PhysRevB.65.144443.

[48] E. Lefrançois, M. Songvilay, J. Robert, G. Nataf, E. Jordan, L. Chaix, C.V. Colin, P. Lejay, A. Hadj-Azzem, R. Ballou, V. Simonet, Magnetic properties of the honeycomb oxide $Na_2Co_2TeO_6$, Phys. Rev. B 94 (2016) 214416. https://doi.org/10.1103/PhysRevB.94.214416.

[49] W. Opechowski, R. Guccione, Magnetism Vol. IIA (1965).

[50] S.V. Streltsov, D.I. Khomskii, Orbital physics in transition metal compounds: new trends, UFN 187 (2017) 1205–1235; Phys. Usp., 60 (2017) 1121–1146. https://doi.org/10.3367/UFNr.2017.08.038196.

[51] M. Reynaud, G. Rousse, J.-N. Chotard, J. Rodríguez-Carvajal, J.-M. Tarascon, Marinite $Li_2M(SO_4)_2$ (M= Co, Fe, Mn) and $Li_1Fe(SO_4)_2$: model compounds for super-super-exchange magnetic interactions, Inorganic Chemistry 52 (2013) 10456-10466. https://doi.org/10.1021/ic401280e.

[52] Daoud-Aladine, B. Kundys, C. Martin, P.G. Radaelli, P.J. Brown, C. Simon, L.C. Chapon, Multiferroicity and spiral magnetism in $FeVO_4$ with quenched Fe orbital moments, Phys. Rev. B 80 (2009) 220402(R). https://doi.org/10.1103/PhysRevB.80.220402.

[53] J.H. Roudebush, N.H. Andersen, R. Ramlau, V.O. Garlea, R. Toft-Petersen, P. Norby, R. Scheider, J.N. Hay, R.J. Cava, Structure and Magnetic Properties of $Cu_3Ni_2SbO_6$ and $Cu_3Co_2SbO_6$ Delafossites with honeycomb lattices, Inorg. Chem. 52 (2013) 6083-6095. https://doi.org/10.1021/ic400415h.

[54] A.I. Kurbakov, A.N. Korshunov, S.Y. Podchezertsev, A.L. Malyshev, M.A. Evstigneeva, F. Damay, J. Park, C. Koo, R. Klingeler, E.A. Zvereva, V.B. Nalbandyan, Zigzag spin structure in layered honeycomb $Li_3Ni_2SbO_6$: A combined diffraction and antiferromagnetic resonance study, Phys. Rev. B 96 (2017) 024417. https://doi.org/10.1103/PhysRevB.96.024417.

1. The atomic structure of $Na_2Ni_2TeO_6$ (*$P6_3/mcm$* sp.gr.) is determined to be different from other compounds of $Na_2M_2TeO_6$ family (M = Co, Zn, Mg) with *$P6_322$* sp.gr. The strong presence of stacking faults defects in layered ordering is found for the first time.
2. For the first time it is detect that the energetically unprofitable Na3 position sandwiched between two TeO_6 octahedra is really empty.
3. The onset of long-range magnetic order was found at T_N = 25±1 K, which is preceded by a short-range order on 2D honeycomb lattice at about 34 K.
4. The ground magnetic state is represented by a commensurate antiferromagnetic zigzag-type structure with the spins that are almost perpendicular to the honeycomb layers and can be described based on so-called J_1 - J_2 - J_3 theoretical model with frustrated exchange interactions in the specified layered honeycomb system.
5. The coherent magnetic scattering area has a disk shape that is homogeneous over the *ab* plane and compressed along the *c*-axis that indicates 2D nature of magnetic correlations in the compound. Restricted along c-axis coherent scattering area and the ESR measurements indicate the quasi-two-dimensional magnetic nature of the compound.